

Thermal conductivity of $\text{Al}_x\text{Ga}_{1-x}\text{N}$ ($0 \leq x \leq 1$) epitaxial layers

Dat Q. Tran ^{1,2,*}, Rosalia D. Carrascon ^{1,2}, Motoaki Iwaya ³, Bo Monemar^{1,2}, Vanya Darakchieva ^{1,2,4,5}
and Plamen P. Paskov ^{1,2,†}

¹Department of Physics, Chemistry, and Biology, Linköping University, 581 83 Linköping, Sweden

²Center for III-Nitride Technology, C3NiT-Janzen, Linköping University, 581 83 Linköping, Sweden

³Faculty of Science and Technology, Meijo University, Nagoya 468-8502, Japan

⁴THz Materials Analysis Center (TheMAC), Linköping University, 581 83 Linköping, Sweden

⁵NanoLund and Solid State Physics, Lund University, 22100 Lund, Sweden



(Received 14 April 2022; accepted 22 September 2022; published 7 October 2022)

$\text{Al}_x\text{Ga}_{1-x}\text{N}$ ternary alloys are emerging ultrawide band gap semiconductor materials for high-power electronics applications. The heat dissipation, which mainly depends on the thermal conductivity of the constituent material in the device structures, is the key for device performance and reliability. However, the reports on the thermal conductivity of $\text{Al}_x\text{Ga}_{1-x}\text{N}$ alloys are very limited. Here, we present a comprehensive study of the thermal conductivity of $\text{Al}_x\text{Ga}_{1-x}\text{N}$ in the entire Al composition range. Thick $\text{Al}_x\text{Ga}_{1-x}\text{N}$ layers grown by metal-organic chemical vapor deposition on GaN/sapphire and GaN/SiC templates are examined. The thermal conductivity measurements are done by the transient thermoreflectance method at room temperature. The effects of the Al composition, dislocation density, Si doping, and layer thickness on the thermal conductivity of $\text{Al}_x\text{Ga}_{1-x}\text{N}$ layers are thoroughly investigated. All experimental data are fitted by the modified Callaway model within the virtual crystal approximation, and the interplay between the different phonon scattering mechanisms is analyzed and discussed.

DOI: [10.1103/PhysRevMaterials.6.104602](https://doi.org/10.1103/PhysRevMaterials.6.104602)

I. INTRODUCTION

Ultrawide band gap semiconductors such as Ga_2O_3 , diamond, and AlN have recently attracted a significant research interest for high-power and high-frequency electronic device applications [1]. The main factor driving this interest is the dependence of the critical electric field for the avalanche breakdown (E_c) on the band gap energy (E_g), which is predicted to be $E_c \sim (E_g)^n$, where $n = 2-2.5$ [2]. The E_c is the key parameter in the figure-of-merit (FOM) of the power electronic device performance [3]; the higher the E_c , the higher the FOM. For $\text{Al}_x\text{Ga}_{1-x}\text{N}$ ternary alloys with a band gap ranging from 3.4 eV to 6 eV, the critical electric field can reach up to 16 MV/cm, implying that the unipolar, lateral, and high-frequency FOMs exceed those of GaN and SiC, the semiconductors that tend to dominate nowadays power electronics [4]. This feature, together with the well-established GaN technology for high electron mobility transistors (HEMTs), makes $\text{Al}_x\text{Ga}_{1-x}\text{N}$ a natural material choice for the next generation power electronic devices.

After the first demonstration of the $\text{Al}_x\text{Ga}_{1-x}\text{N}$ -channel HEMT [5] many groups have reported $\text{Al}_x\text{Ga}_{1-x}\text{N}/\text{Al}_y\text{Ga}_{1-y}\text{N}$ lateral devices with good gate control, leakage current, and ohmic contacts (for a review see Ref. [4]). Recently, a record 3000 V breakdown voltage has been demonstrated in a Schottky-drain $\text{Al}_{0.3}\text{Ga}_{0.7}\text{N}/\text{Al}_{0.1}\text{Ga}_{0.3}\text{N}$ HEMT [6]. Also, Al-rich $\text{Al}_x\text{Ga}_{1-x}\text{N}$ -channel HEMTs with a cutoff frequency up to 40 GHz have been reported [7,8], illustrating the promise of these devices for high-frequency applications. Quasivertical $\text{Al}_x\text{Ga}_x\text{N}$ devices, such as the 1600 V $\text{Al}_{0.3}\text{Ga}_{0.7}\text{N}$ p - i - n diode [9] and $\text{Al}_{0.3}\text{Ga}_{0.7}\text{N}$ Schottky diode with a breakdown voltage of 500 V [10], have also been demonstrated.

As the $\text{Al}_x\text{Ga}_{1-x}\text{N}$ -based devices target an operation at high powers (i.e., at high currents and high voltages), the Joule heat generation becomes a problem for the device performance and reliability. The self-heating leads to an increased junction temperature which not only reduces the electron mobility and saturation velocity, but also causes a thermal device degradation. The self-heating has been extensively studied in $\text{Al}_x\text{Ga}_{1-x}\text{N}/\text{GaN}$ HEMTs and shown to cause a current degradation as well as a thermal-induced reduction of the breakdown voltage [11–14]. The self-heating in $\text{Al}_x\text{Ga}_{1-x}\text{N}$ -based devices has been not well explored. Recently, it has been shown that the self-heating problem in $\text{Al}_x\text{Ga}_{1-x}\text{N}$ -channel HEMTs is more severe than that in GaN-channel HEMTs because of the anticipated lower thermal conductivity in $\text{Al}_x\text{Ga}_{1-x}\text{N}$ alloys [15,16]. Then, for proper device thermal management it is necessary to know the accurate thermal conductivity of $\text{Al}_x\text{Ga}_{1-x}\text{N}$ thin and thick layers used in the

*dat.tran@liu.se

†plamen.paskov@liu.se

Published by the American Physical Society under the terms of the Creative Commons Attribution 4.0 International license. Further distribution of this work must maintain attribution to the author(s) and the published article's title, journal citation, and DOI. Funded by Bibsam.

device structures, and more importantly to figure out the reason for low thermal conductivity in this material.

Thermal conductivity of GaN and AlN has been extensively studied in the past. For bulk GaN grown by hydride vapor phase epitaxy (HVPE) and high-pressure, high-temperature and amonothermal growth, a room-temperature thermal conductivity of 225–270 W/m K has been reported [17–24]. These values are close to those obtained from the first-principles calculations (239–335 W/m K) for a defect-free GaN crystal [25–28]. Lower thermal conductivity has been measured in doped GaN with an impurity concentration above 10^{18} cm⁻³ which is attributed to the increased phonon-point-defect scattering and to the phonon-free-carrier scattering in *n*-type material [20,21,29,30]. The reported experimental data for room-temperature thermal conductivity of bulk AlN grown by HVPE and physical vapor transport, and of thick (>15 μm) layers grown by metal-organic chemical vapor deposition (MOCVD), range between 270 W/m K and 374 W/m K [17,31–35]. The large variation in data could be explained by the difference in the background impurity concentration in the measured samples. First-principles calculations have predicted a thermal conductivity of 290–569 W/m K of pure AlN [27,36,37].

There are several reports on the thermal conductivity of Al_{*x*}Ga_{1-*x*}N alloys. Layers with Al composition up to $x = 0.44$ grown by MOCVD and HVPE on *c*-plane sapphire have been examined by time-domain thermoreflectance (TDTR) and 3ω methods [38–41]. In all cases, a strong reduction of the room-temperature thermal conductivity was found with increasing Al composition. For example, a value of 25 W/m K has been measured in Al_{0.4}Ga_{0.6}N layers [39], which is about 10 times smaller than that of bulk GaN. Recently, we have reported on the thermal conductivity in high Al content Al_{*x*}Ga_{1-*x*}N layers grown on SiC and found that already for $x = 0.9$ the thermal conductivity drops more than 5 times compared to the value of AlN layers of the same thickness [42]. Thermal conductivity data for low and high Al content Al_{*x*}Ga_{1-*x*}N buffer layers in HEMTs showing values below 10 W/m K have been also reported [16]. Although the thermal conductivity of thin heteroepitaxial layers is expected to be lower than that of bulk materials due to the phonon-dislocation and phonon-boundary scattering, the main reason for lower values measured in Al_{*x*}Ga_{1-*x*}N is the phonon-alloy scattering, i.e., the phonon scattering by the perturbations in mass and size of the constituent atoms in the alloy. This has been confirmed by our study of the thickness dependence of the thermal conductivity in Al_{*x*}Ga_{1-*x*}N layers grown by HVPE [43]. The first-principles calculations for intrinsic Al_{*x*}Ga_{1-*x*}N have also shown a dominant contribution of the phonon-alloy scattering on the thermal conductivity [26,44]. A detailed study of the thermal conductivity of Al_{*x*}Ga_{1-*x*}N alloys in a wide range of Al compositions is still missing, however. Moreover, the interplay between the phonon-alloy scattering and the phonon-point-defect and phonon-dislocation scattering have never been examined.

In this work, we present a systematic study of the thermal conductivity of Al_{*x*}Ga_{1-*x*}N in the entire composition range. The experimental results are interpreted within the frame of a modified Callaway model where all phonon-scattering processes are explicitly accounted for. A refined treatment of

the phonon-alloy scattering is suggested and included in the model. The effect of dislocation density and Si doping on the thermal conductivity is experimentally revealed and discussed along with theoretical modeling. Finally, we investigate the role of layer surface roughness on the thermal boundary resistance (TBR) at the metal/Al_{*x*}Ga_{1-*x*}N interface.

II. EXPERIMENTAL

We have studied two sets of Al_{*x*}Ga_{1-*x*}N samples (see Table I). Set 1 (grown at the Akasaki Institute, Meijo University, Nagoya, Japan) includes 1.5–4.3 μm thick layers with low Al composition ($x < 0.1$) grown by MOCVD on 2 μm undoped GaN on *c*-plane sapphire. Some of these layers are doped with Si with a concentration up to 5×10^{20} cm⁻³ [45]. Hall effect measurements at room temperature in doped samples reveal a complete donor ionization; i.e., the free-electron concentration equals the Si concentration. The samples in set 2 (grown at our MOCVD laboratory, IFM, Linköping University, Sweden) are nominally undoped Al_{*x*}Ga_{1-*x*}N ($x = 0.57$ –1) grown by hot-wall MOCVD on 4H-SiC substrate with a 100 nm graded Al_{*x*}Ga_{1-*x*}N buffer. The growth of these layers implements the previously developed recipes for high crystal quality Al_{*x*}Ga_{1-*x*}N and AlN epitaxial layers [46–48]. In order to calibrate the effect of dislocation density on the thermal conductivity, bulk GaN samples grown by HVPE were also examined.

The dislocation density and the Al composition in all studied samples were estimated by high-resolution x-ray diffraction (XRD) measurements. The measurements were performed in triple-axis configuration with an incident beam optics of hybrid monochromator 2-bounce Ge(220) and a diffracted beam optics of 3-bounce Ge(220). Except for the GaN substrates for which the x-ray beam is focused in a point with diameter of 1 mm, the x-ray beam has a line shape with a dimension of 10 × 1 (mm × mm). The surface morphology is studied by atomic force microscopy (AFM). The layer thicknesses were measured by ultraviolet-visible spectroscopy ellipsometry and cross-section scanning electron microscopy. The free-electron concentration in Si-doped layers was determined by conventional Hall-effect measurements. It was found that at room temperature the free-electron concentration equals the Si concentration.

The thermal conductivity measurements were done by transient thermoreflectance (TTR) at room temperature. The system we have used comprises a pump-pulsed Nd:YAG laser (532 nm) with 8 ns pulse duration and a repetition rate of 50 Hz and a probe continuous-wave Ar laser (488 nm). The pump laser heats the sample through a 200 ± 5 nm thick gold (Au) transducer deposited on the top sample surface. The power of the pump laser is much larger than that of the probe laser, so the heating due to the probe laser has a negligible effect. The spot size of the pump and probe laser beams is 200 μm and 15 μm, respectively, ensuring that the heat transport along the direction perpendicular to the sample surface (i.e., along the *c* axis) is probed in the experiment.

In the experiments, the decay of the probe laser beam reflectance from the Au transducer after the pump laser pulse is measured. Since the change of the Au reflectance is linearly proportional to the temperature [49], the decay of the

TABLE I. Al composition (x), thickness (L), screw (D_S), and edge (D_E) dislocation densities, and thermal conductivity (k) measured at 300 K of the studied samples.

Samples		Al content (x)	L (μm)	D_S (cm^{-2})	D_E (cm^{-2})	N_{Si} (cm^{-3})	k at 300 K (W/m K)
AlGa _N (set 1)	AL0-1	0	4.0	9.0×10^7	1.7×10^9	1×10^{17}	152
	AL0-2	0	4.3	8.0×10^7	1.6×10^9	9×10^{18}	149
	AL0-3	0	4.3	9.0×10^7	1.6×10^9	5×10^{19}	151
	AL1-1	0.01	1.9	1.0×10^8	1.5×10^9	3×10^{17}	60.7
	AL1-2	0.01	1.9	1.0×10^8	1.5×10^9	2×10^{18}	67.0
	AL1-3	0.01	1.9	1.0×10^8	1.5×10^9	2×10^{19}	77.6
	AL3-1	0.03	2.2	1.5×10^8	1.4×10^9	3×10^{17}	38.0
	AL3-2	0.03	1.4	2.0×10^8	2.0×10^9	2×10^{20}	42.0
	AL3-3	0.03	1.6	2.0×10^8	2.0×10^9	5×10^{20}	41.5
	AL4-1	0.04	1.7	2.0×10^8	1.5×10^9	2×10^{17}	33.0
	AL4-2	0.04	1.5	2.0×10^8	2.0×10^9	1×10^{18}	33.9
	AL4-3	0.04	1.5	2.0×10^8	2.0×10^9	1×10^{19}	38.3
	AL4-4	0.04	1.5	2.0×10^8	2.0×10^9	6×10^{19}	42.2
	AL9	0.09	1.5	1.7×10^8	1.9×10^9	5×10^{17}	21.5
AlGa _N (set 2)	S1	0.57	1.20	2.9×10^8	5.6×10^9	$<5 \times 10^{16}$	8.8
	S2	0.62	1.4	2.9×10^8	5.5×10^9	$<5 \times 10^{16}$	6.7
	S3	0.78	1.0	3.0×10^8	5.5×10^9	$<5 \times 10^{16}$	7.7
	S4	0.85	0.45	6.0×10^7	2.9×10^9	$<5 \times 10^{16}$	10.0
	S5	0.88	0.45	1.7×10^8	3.4×10^9	$<5 \times 10^{16}$	9.5
	S6	1	0.45	4.0×10^8	4.0×10^9	$<5 \times 10^{16}$	84
Ga _N (bulk)	G-B1	0	800	1.0×10^6	2.0×10^7	$<5 \times 10^{16}$	225
	G-B2	0	800	2.0×10^7	1.3×10^8	$<5 \times 10^{16}$	215
	G-B3	0	800	6.0×10^7	4.8×10^8	$<5 \times 10^{16}$	200
	G-B4	0	1000	1.0×10^7	7.0×10^8	8×10^{18}	180
	G-B5	0	1000	2.0×10^8	1.2×10^9	1×10^{18}	155

reflectance corresponds to the decay of the sample temperature. The transients of the sample temperature are analyzed by the one-dimensional heat transport equation [50]. The heat source in this equation is determined by the heating of the Au transducer and depends on the pump laser fluence, and the absorption and reflectivity of Au at the pump laser wavelength. Note that the transducer layer is of sufficient thickness and the pump laser beam does not penetrate in underlying layers. Other input parameters in the analysis are the thicknesses of the Au transducer and $\text{Al}_x\text{Ga}_{1-x}\text{N}$ layers, the specific heat capacities (C_p) of Au and $\text{Al}_x\text{Ga}_{1-x}\text{N}$, and the thermal conductivity of Au. The C_p of $\text{Al}_x\text{Ga}_{1-x}\text{N}$ is assumed to depend linearly on the composition between the values for GaN [51] and AlN [52].

The thermal conductivity of GaN/sapphire and graded $\text{Al}_x\text{Ga}_{1-x}\text{N}/\text{SiC}$ templates was initially measured and also used as an input parameter. Due to the low temperature rise in the experiment (<30 K), all input parameters are taken to be independent of temperature. The thermal conductivity of $\text{Al}_x\text{Ga}_{1-x}\text{N}$ layers is obtained via a least-squares fit of the probe laser beam reflectance transients by the solution of the one-dimensional heat transport equation. In the fitting procedure, two fitting parameters are used, the layer thermal conductivity and the thermal boundary resistance at the Au/layer or layer/template interface.

III. THEORETICAL MODEL

The general description of the lattice thermal conductivity in solids is based on solving the phonon Boltzman

transport equation (BTE). First-principles calculations, which implement a self-consistent solution for the phonon distribution and incorporate the quantum mechanical phonon-phonon scattering processes, have the advantage of providing purely predictive thermal conductivity in pure materials [53]. However, this approach is very challenging to apply for disordered and doped materials due to the complexity and high computational cost. The solution of the phonon BTE can be simplified by using the relaxation time approximation, which is the basis of the Callaway model [54], commonly used to describe the thermal conductivity in semiconductors. The application of the Callaway model relies on the fit of the temperature-dependent experimental data with few adjustable parameters and offers a flexible way to calculate the thermal conductivity in pure and defective materials using easily implemented formulation of various phonon scattering rates.

The experimental thermal conductivity data in this work were analyzed in the framework of a so-called modified Callaway model, which takes into account the individual contributions of the longitudinal (LA) and transverse (TA) acoustic phonon scattering [55–57]. In this model, Debye-like dispersion is assumed for the acoustic phonons and various phonon scattering processes are taken into account via frequency and temperature dependent scattering rates. Then, the thermal conductivity is given by [56,57]

$$k = k_1 + k_2, \quad (1)$$

where

$$k_1 = \sum_s \frac{k_B^4}{6\pi^2 \hbar^3 v_s} T^3 \int_0^{\theta_D^s/T} \tau_C^s \frac{y^4 \exp(y)}{[\exp(y) - 1]^2} dy, \quad (2)$$

$$k_2 = \sum_s \frac{k_B^4}{6\pi^2 \hbar^3 v_s} T^3 \frac{\left[\int_0^{\theta_D^s/T} \frac{\tau_C^s}{\tau_N^s} \frac{y^4 \exp(y)}{[\exp(y) - 1]^2} dy \right]^2}{\left[\int_0^{\theta_D^s/T} \frac{\tau_C^s}{\tau_N^s \tau_R^s} \frac{y^4 \exp(y)}{[\exp(y) - 1]^2} dy \right]}. \quad (3)$$

Here, k_B is the Boltzmann constant, T is the temperature, \hbar is the reduced Planck constant, v_s is the acoustic phonon velocity, and θ_D^s is the Debye temperature. The integral variable is $y = \hbar\omega/k_B T$, where ω is the phonon frequency. The summation is over the three acoustic phonon modes in wurtzite crystals—one longitudinal and two transverse, i.e., $s = \text{LA, TA1, TA2}$. Note that for heat propagation along the c axis (which is the case of the measurements in this work), the two transverse modes are degenerated. The phonon velocities are given by $v_{\text{LA}} = (C_{33}/\rho)^{1/2}$ and $v_{\text{TA1}} = v_{\text{TA2}} = (C_{44}/\rho)^{1/2}$, where C_{ij} are the elastic constants and ρ is the density. The Debye temperatures are determined from the zone boundary frequencies at the A symmetry point of the Brillouin zone ω_{max}^s by $\theta_D^s = \hbar\omega_{\text{max}}^s/k_B$ [57].

In Eqs. (2) and (3) τ_N^s denotes the relaxation time for normal (N) phonon scattering which is a nonresistive process, τ_R^s is the relaxation time for all resistive (R) scattering processes, and τ_C^s is the combined relaxation time given by $(\tau_C^s)^{-1} = (\tau_N^s)^{-1} + (\tau_R^s)^{-1}$. The resistive scattering processes considered in the model include the umklapp (U) phonon-phonon scattering, the phonon-isotope (I) scattering, the phonon-point-defect (PD) scattering, the phonon-dislocation (D) scattering, the phonon-alloy (A) scattering, the phonon-free-electron (FE) scattering, and the phonon-boundary (B) scattering. Then, Matthiessen’s rule is applied for τ_R^s by $(\tau_R^s)^{-1} = (\tau_U^s)^{-1} + (\tau_I^s)^{-1} + (\tau_{PD}^s)^{-1} + (\tau_D^s)^{-1} + (\tau_A^s)^{-1} + (\tau_{FE}^s)^{-1} + (\tau_B^s)^{-1}$.

N scattering is a three-phonon scattering process in which the phonon momentum is conserved meaning that this process does not contribute to thermal resistance. However, N scattering does impact the phonon distribution and then affects all resistive processes. The general form of N-scattering process is expressed by [21,57,58]

$$(\tau_N^s)^{-1} = \left(\frac{k_B}{\hbar}\right)^{a+b} \frac{\hbar(\gamma_s)^2 (V_o)^{(a+b-2)/3}}{M(v_s)^{a+b}} y^a T^{a+b}, \quad (4)$$

where M is the average atomic mass, $V_o = a^2 c \sqrt{3}/8$ is the average volume per atom (a and c are the lattice constants), and γ_s are the Grüneisen parameters of phonon branches which describe the anharmonicity of the crystal lattice. In the case of wurtzite crystals like $\text{Al}_x\text{Ga}_{1-x}\text{N}$, $(a, b) = (2, 1)$ for LA phonons and $(a, b) = (1, 1)$ for TA phonons at room temperatures [57].

U scattering is also a three-phonon scattering process; it is, however, thermally resistive. Furthermore, this process gives the major resistive contribution to the thermal transport in defect-free crystals, and leads to a characteristic exponential decay of thermal conductivity proportional to T^{-1} at high temperatures. The form of U-scattering rate is written as

[21,57]

$$(\tau_U^s)^{-1} = \frac{k_B^2 (\gamma_s)^2}{\hbar M (v_s)^2 \theta_D^s} \exp\left(-\frac{\theta_D^s}{3T}\right) y^2 T^3. \quad (5)$$

I scattering is a result of the atomic mass fluctuation when various isotopes of the constituent chemical elements are present in the material. In semiconductors, this scattering process is shown to be significant at low temperatures and to reduce the maximum thermal conductivity (typically occurring at $T \approx 0.05\theta_D^s$) by 30%–50% [56,57]. In the high-temperature range ($T > 180$ K for GaN and $T > 250$ K for AlN), the I-scattering process still affects the thermal conductivity in undoped or low-doped semiconductors. The I-scattering rate is expressed by [57,59]

$$(\tau_I^s)^{-1} = \left(\frac{k_B}{\hbar}\right)^4 \frac{V_o}{4\pi(v_s)^3} \Gamma_I y^4 T^4. \quad (6)$$

For ternary compounds the strength of the phonon-isotope scattering Γ_I can be written as

$$\Gamma_I = 2 \sum_i \left(c_i \frac{M_i}{M_{\text{tot}}}\right)^2 \Gamma_i, \quad (7)$$

where Γ_i is the scattering parameter for each single chemical element ($i = \text{Ga, Al, N}$), M_i is the atomic mass, c_i is the corresponding fractional composition (i.e., c_i is x for Al, $1 - x$ for Ga, and 1 for N), and $M_{\text{tot}} = xM_{\text{Al}} + (1 - x)M_{\text{Ga}} + M_{\text{N}}$, where x is the Al composition. Γ_i scattering parameters are given by [57]

$$\Gamma_i = \sum_j d_j^i \left(\frac{m_j^i - M_i}{M_i}\right)^2 \quad (8)$$

with

$$M_i = \sum_j d_j^i m_j^i, \quad (9)$$

where m_j^i is the atomic mass of the j th isotope and d_j^i is the fractional atomic natural abundance.

PD scattering originates from the lattice disorder caused by point defects which can be substitutional impurities or vacancies. The expression for the PD-scattering rate is written as [21,59]

$$(\tau_{PD}^s)^{-1} = \left(\frac{k_B}{\hbar}\right)^4 \frac{V_o}{4\pi(v_s)^3} \Gamma_{PD} y^4 T^4, \quad (10)$$

where Γ_{PD} is the the strength of the PD scattering. In this scattering process, the phonons are scattered by (i) mass fluctuation between the host atom and the impurity (vacancy), (ii) the change in the force constant of the bonds neighboring to the defect, and (iii) the strain field caused by the size difference between the host atom and the impurity (vacancy). Due to the lack of information about the force constant in $\text{Al}_x\text{Ga}_{1-x}\text{N}$ the contribution of the force-constant term is assumed to be equal to that of the strain-field term. Then, Γ_{PD} can be written as [21,59]

$$\Gamma_{PD} = \sum_p f_p \left[\left(\frac{M_p - M}{M}\right)^2 + 8(\gamma_s)^2 (1 + Q)^2 \left(\frac{\Delta R_p}{R}\right)^2 \right], \quad (11)$$

where f_p and M_p are the fractional concentration and the atomic mass of the p th impurity, ΔR_p is the average local displacement in the host lattice due to the p th impurity, and R is the average nearest-neighbor atomic radius in the host crystal. The displacement ΔR_p is calculated from the difference between the average bond length in the host crystal and the average bond length in the presence of an impurity in a relaxed lattice. The constant Q equals 4.2 assuming that the nearest-neighbor bonds of the impurity have the same anharmonicity as the bonds in host crystal [59].

D scattering arises from the phonon scattering on both the core of dislocation lines and the elastic strain field on the dislocation lines. Taking into account the contributions of edge and screw dislocations, the total D-scattering rate is given by [59,60]

$$(\tau_D^s)^{-1} = (\tau_{\text{core}}^s)^{-1} + (\tau_{\text{strain}}^s)^{-1}, \quad (12)$$

where

$$(\tau_{\text{core}}^s)^{-1} = \eta N_D \left(\frac{k_B}{\hbar} \right)^3 \frac{V_o^{4/3}}{(v_s)^2} y^3 T^3, \quad (13)$$

$$(\tau_{\text{strain}}^s)^{-1} = 0.06 \eta \left(\frac{k_B}{\hbar} \right) (\gamma_s)^2 [N_S b_S^2 + N_E b_E^2 P_E^2] y T, \quad (14)$$

and

$$P_E^2 = \frac{1}{2} + \frac{1}{24} \left(\frac{1 - 2\sigma}{1 - \sigma} \right)^2 \left[1 + \sqrt{2} \left(\frac{v_L}{v_T} \right) \right]^2. \quad (15)$$

The $(\tau_{\text{core}}^s)^{-1}$ and $(\tau_{\text{strain}}^s)^{-1}$ are the scattering rates from the dislocation core and the elastic strain field, respectively. In Eqs. (13)–(15), N_D is the total dislocation density, N_S and N_E are the densities of screw and edge dislocations, respectively, η is the weight factor accounting for the mutual orientation of the dislocation line and the direction of the heat transport (assumed to be 0.55 for a random distribution of all dislocation [60]), b_S and b_E are the Burgers vectors for the screw and edge dislocations, and $\sigma = C_{13}/(C_{11} + C_{12})$ is the Poisson ratio. Numerical calculations using Eqs. (12)–(15) give a threshold dislocation density (i.e., the density at which the thermal conductivity starts to decrease) in the range of 10^{10} – 10^{11} cm^{-2} [60]. However, the experimental data for GaN [18,61] indicate that the threshold dislocation density is much lower. Then, we add a dimensionless scaling factor on the right side of Eq. (12) in order to match the experimentally determined threshold density. Paskov *et al.* [21] have proposed a scaling factor of 1000. Based on the analysis of our new data for the dislocation density dependence of the thermal conductivity of bulk GaN (see Sec. IV E) we have obtained a scaling factor of 400, which value is used in this work.

A scattering is described in the framework of the virtual crystal approximation (VCA), in which the disordered alloy is replaced by an ordered virtual crystal with virtual atomic mass, atomic volume, and lattice constants [40,62,63]. Then, the phonons are scattered by the perturbations of the virtual crystal. Due to the relatively small lattice mismatch between GaN and AlN [64] and the low critical temperature for the miscibility gap (much lower than the growth temperature) [65], there is an excellent solubility for $\text{Al}_x\text{Ga}_{1-x}\text{N}$ and no inhomogeneous Al/Ga distribution or segregation is expected.

Then, the VCA approach is well justified for $\text{Al}_x\text{Ga}_{1-x}\text{N}$ alloys. The expression for the A-scattering rate is similar to that for the PD-scattering rate, but modified to take into account the coexistence of the substitutional Al into the GaN lattice and substitutional Ga into the AlN lattice:

$$(\tau_A^s)^{-1} = \left(\frac{k_B}{\hbar} \right)^4 \frac{V_o}{4\pi(v_s)^3} \Gamma_A y^4 T^4, \quad (16)$$

where

$$\Gamma_A(x) = \sum_l c_l \left[\left(\frac{\Delta M_l}{M(x)} \right)^2 + 8[\gamma_s(x)]^2 (1 + Q)^2 \left(\frac{\Delta R_l}{R(x)} \right)^2 \right]. \quad (17)$$

Here, the index l denotes group-III atomic constituents (Ga and Al), c_l is the atomic fractional compositions, $\Delta M_l = M_l - M(x)$, $\Delta R_l = R_l - R(x)$, $M(x) = xM_{\text{Al}} + (1-x)M_{\text{Ga}}$, and $R(x) = xR_{\text{Al}} + (1-x)R_{\text{Ga}}$. $M(x)$ and $R(x)$ are the averaged atomic mass and atomic radius, respectively, and $\gamma_s(x)$ are the mode Grüneisen parameters of $\text{Al}_x\text{Ga}_{1-x}\text{N}$ alloy. The second term in Eq. (17) combines the difference in the atomic radius and the difference in the stiffness constant of the nearest-neighbor bonds [21]. Assuming that the incorporation of Al (Ga) into GaN (AlN) does not change significantly the anharmonicity of nearest-neighbor bonds, the parameter Q has a value of 4.2 [59].

FE scattering is believed to give a negligible contribution to the thermal conductivity in undoped and low-doped semiconductors. In the case of GaN, the FE scattering was shown to start playing a role at electron concentrations above 10^{17} cm^{-3} [21]. Within the effective mass approximation, the FE-scattering rate is formulated by [66,67]

$$(\tau_E^s)^{-1} = \frac{E_1^2(m_e^2)k_B T}{2\pi\hbar^4\rho v_s} \left[y - \ln \left(\frac{1 + \exp(Z + y/2)}{1 + \exp(Z - y/2)} \right) \right] \quad (18)$$

and

$$Z = \frac{y^2 k_B T}{8m_e(v_s)^2} + \frac{m_e(v_s)^2}{2k_B T} - \frac{E_F}{k_B T}, \quad (19)$$

where E_1 the deformation potential for the electron-acoustic-phonon interaction, m_e the electron effective mass, and E_F the Fermi-level energy measured from the conduction band edge.

In bulk materials and thick layers, B scattering is important only at very low temperatures, where the phonon mean free path (MFP) becomes comparable to the dimensions of the sample under investigation [68,69]. In thin layers, however, the contribution of this scattering process to the thermal conductivity is significant even at room temperatures. The B-scattering rate is assumed to be independent of temperature and phonon frequency and can be expressed as [61,70]

$$(\tau_B^s)^{-1} = \frac{v_s}{aL}, \quad (20)$$

where L is the layer thickness and a is a dimensionless parameter. aL can be regarded as an effective MFP along the direction of the heat transport which is essentially determined by the size effect. A value of 2.38 for the a parameter has been found by fitting Eq. (20) with the solution of the Boltzmann

TABLE II. Material parameters of GaN and AlN used in the thermal conductivity calculations.

Materials properties		GaN	AlN
Density [71] (kg/m ³)	ρ	6195	3230
Lattice constants [72,73] (Å)	a	3.1893	3.1120
	c	5.1852	4.9809
Elastic constant [74,75] (GPa)	C_{11}	359.4	401.2
	C_{12}	129.2	135
	C_{13}	92	96.3
	C_{33}	389.9	368.2
	C_{44}	98	122.6
Acoustic phonon velocity (m/s)	v_L	7933	10677
	v_T	3997	6161
Phonon frequency at Brillouin zone boundary [76,77] (THz)	ω_{\max}^L	43.54	64.21
	ω_{\max}^T	20.73	32.99
Debye temperature (K)	θ_D^L	333	490
	θ_D^T	158	252
Average atomic volume per atom (m ³)	V_o	1.142×10^{-29}	1.044×10^{-29}
Average atomic mass (natural) (kg)	M	6.952×10^{-26}	3.4031×10^{-26}
Average atomic radius (Å)	R	0.9752	0.9470
Poisson ratio	σ	0.188	0.180
Electron effective mass [78] (m_o)	m_e	0.2	0.32
Acoustic phonon deformation potential [79] (eV)	E_1	8.3	9.5
Grüneisen parameter (extracted)	γ_L	0.64	0.75
	γ_T	0.31	0.35

transport equation for a thin layer [61] and used to model the thickness dependence of the thermal conductivity of GaN [61,70]. In our analysis, we use $a = 1.5$, the value extracted from the experimental thickness dependence of the thermal conductivity of $Al_xGa_{1-x}N$ with various compositions [43].

Finally, the thermal conductivity is calculated from Eqs. (1)–(3) by inserting the expressions for all scattering rates [Eqs. (4)–(20)]. All material parameters of GaN and AlN needed in the model are summarized in Table II. For $Al_xGa_{1-x}N$ alloys a linear interpolation between the values of binary compounds is used.

IV. RESULTS AND DISCUSSION

A. Al composition analysis

Figure 1 shows XRD 2θ - ω scans with respect to the (0002) plane for all studied $Al_xGa_{1-x}N$ layers. The variation of peak position indicates the change in the c lattice constant at different Al compositions. The a lattice constant was determined from the position of (10 $\bar{1}$ 2) diffraction peaks and the measured c lattice constant. Using Vegard’s law for the lattice constants and the elastic constants, the relation between the out-of-plane and in-plane strain state in the $Al_xGa_{1-x}N$ alloy is described by [80]

$$C_{33}(x) \frac{c_m(x) - c(x)}{c(x)} + 2C_{13}(x) \frac{a_m(x) - a(x)}{a(x)} = 0, \quad (21)$$

where $c_m(x)$ and $a_m(x)$ are the measured lattice constants and $c(x)$ and $a(x)$ are the fully relaxed lattice constants for Al composition x . Any value of x that satisfies Eq. (21) returns Al composition. Applying this analysis, the Al content in all studied $Al_xGa_{1-x}N$ layers is determined and listed in Table I. The Al compositions obtained from XRD were confirmed by SIMS measurements.

B. Dislocation density analysis

Densities of screw and edge dislocations were determined from of XRD rocking-curve scans. For screw dislocation density estimation, the William-Hall (W-H) method, where $\beta \sin(\theta)/\lambda$ is plotted as a function of $\sin(\theta)/\lambda$ for three symmetric reflections (0002), (0004), and (0006), was applied [81]. β is the integral width of the measured profile, λ is the x-ray wavelength, and 2θ is the scattering angle. The

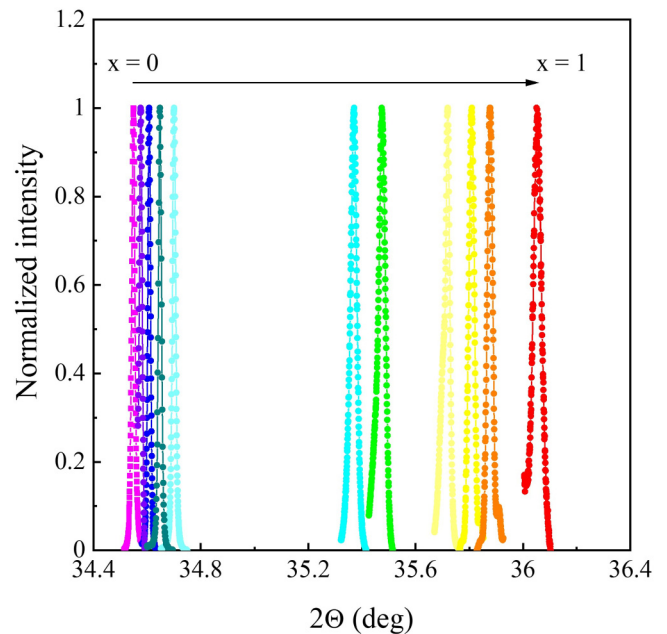


FIG. 1. XRD 2θ - ω scans for (0002) peaks of all studied $Al_xGa_{1-x}N$ layers.

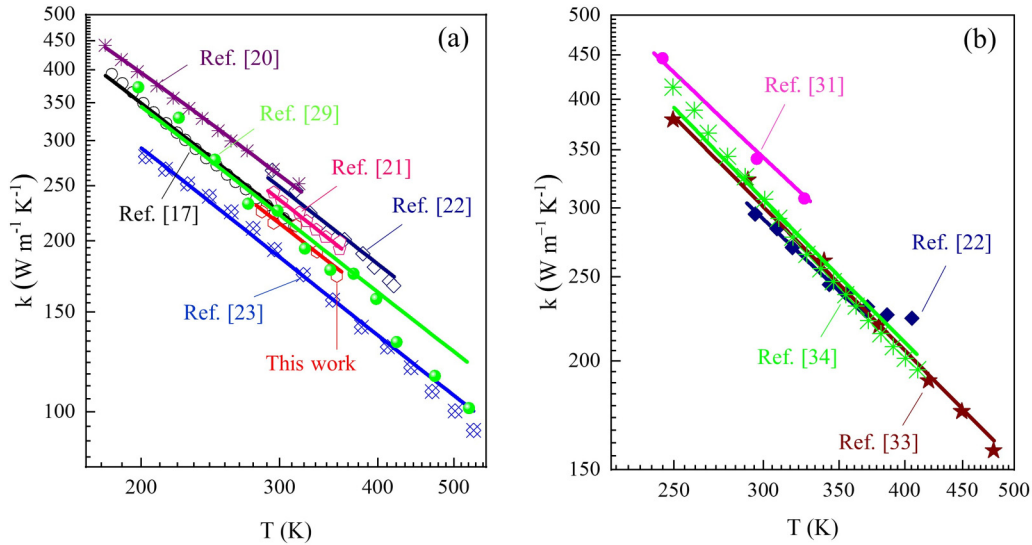


FIG. 2. Experimental thermal conductivity data (symbols) and the fit (lines) by the model described in Sec. III for (a) GaN and (b) AlN. The Grüneisen parameters γ_L and γ_T are the only fitting parameters used.

correlation length parallel to the sample surface was estimated from the y intercept y_o of the fitted line by $L_{||} = 0.9/2y_o$ [81]. The slope is a direct measure of the tilt angle α_S .

As for the edge dislocations, the twist angle α_E was obtained from the plot of the reflection peak broadening versus the inclination angle from the surface normal [82]. Reflection from the symmetric plane (0002) and five asymmetric planes (10 $\bar{1}$ 1), (10 $\bar{1}$ 2), (10 $\bar{1}$ 3), (10 $\bar{1}$ 4), and (10 $\bar{1}$ 5) were measured. In the fitting, the tilt angle obtained from the W-H plot was used as a fixed parameter.

Finally, the dislocation densities are calculated by

$$D_i = \frac{\alpha_i^2}{4.35b_i^2}, \quad (22)$$

where $i = S, E$, and $b_S = c$ and $b_E = a$ are the Burger vectors for screw and edge dislocations, respectively [81,82]. The values obtained for all studied samples are shown in Table I.

C. Grüneisen parameters

The calculation of the lattice thermal conductivity using the theoretical model described in Sec. III requires a number of material parameters. In the case of GaN and AlN, all these parameters, except for the Grüneisen parameters, are well known from numerous experimental and theoretical studies (Table II). The phonon-mode Grüneisen parameters describe the anharmonicity of the atomic interactions in the crystal lattice and determine the strength of the phonon-phonon scattering. PD-, D-, and A-scattering rates are also affected by the crystal lattice anharmonicity. Generally, the Grüneisen parameters depend on the phonon frequency, but in the Callaway model the average-mode parameters are used [57]. The only available experimental data for the Grüneisen parameters in GaN and AlN are those obtained from thermal expansion measurements [83,84]. In these studies, however, the extracted values correspond to the average anharmonicity of the entire phonon spectrum and no distinction between the different phonon modes can be made.

Here, the relevant Grüneisen parameters γ_L and γ_T are obtained by a least-squares minimization fit of the available experimental data for the temperature dependence (above 200 K) of thermal conductivity of bulk GaN and AlN. The fit was done by the modified Callaway model (described in Sec. III) using γ_L and γ_T as the only fitting parameters. The fitting is illustrated in Fig. 2. At high-temperature range, the temperature dependence of the thermal conductivity can be approximated by $k \propto T^{-m}$. Note that for defect-free semiconductor crystals, where the umklapp phonon scattering dominates, a slope of $m \approx 1$ is expected. The extracted Grüneisen parameters together with the values of m for different sets of data are given in Table III.

In the case of AlN, a good fit could be achieved only in a narrow temperature range [Fig. 2(b)]. This can be explained by the smaller energy gap between acoustic and optical phonon branches in AlN [85], which results in a strong contribution of the three-phonon scattering process involving the optical phonons at higher temperatures [36,37]. In the modified Callaway model used in the fitting of the experimental data only the acoustic phonons are considered, however. This is also the reason for the higher values obtained for m . For GaN, the acoustic-optical phonon gap is larger and the contribution of the three-phonon scattering process involving the optical phonons is negligible. Thus, a quite satisfactory fit in a wide temperature range is achieved [Fig. 2(a)].

The extracted Grüneisen parameters for GaN and AlN show rather good agreement between the different sets of experimental data. For later calculations, we use $\gamma_L = 0.64$ and $\gamma_T = 0.31$ for GaN, and $\gamma_L = 0.75$ and $\gamma_T = 0.35$ for AlN. For $\text{Al}_x\text{Ga}_{1-x}\text{N}$ alloys, a linear interpolation between the values of binary compounds is used.

D. Effect of the phonon-alloy scattering

The thermal conductivity of all $\text{Al}_x\text{Ga}_{1-x}\text{N}$ samples measured at 300 K is shown in Fig. 3. The samples of set 1 are epitaxial layers with a low Al composition ($0 \leq x \leq$

TABLE III. Grüneisen parameters, γ_L and γ_T , extracted by fitting of the experimental temperature dependence of the thermal conductivity of GaN and AlN.

Reference	Method	Impurity concentration ($\times 10^{16} \text{ cm}^{-3}$)	Dislocation density (cm^{-2})	γ_L	γ_T	m	
GaN	[17]	Steady-state heat flow	[O] = 2.1, [Si] = 0.4	5×10^4	0.64	0.31	1.17
	[20]	Steady-state heat flow	[O] = 4	5×10^4	0.46	0.56	1.00
	[21]	3ω	[O] = 2.3, [Si] = 1.6, [C] = 0.7	5×10^6	0.56	0.36	1.17
	[22]	3ω	[O] = 1.0, [Si] = 10, [C] = 1.0	5×10^4	0.60	0.30	1.3
	[23]	TDTR	[O] = 100	2.1×10^6	0.61	0.45	1.12
	[29]	3ω	[O] = 230, [Mg] = 230	1×10^4	0.63	0.33	1.33
Present work	TTR	[Si] = 10	5×10^6	0.65	0.31	1.08	
AlN	[22]	3ω	[O] = 10, [Si] = 2, [C] = 5	1×10^3	0.75	0.40	1.2
	[31]	3ω	[O] = 3.1, [Si] = 2.8, [C] = 4.6	1×10^3	0.90	0.30	1.32
	[33]	TDTR	[O] = 33, [Si] = 1, [C] = 14	1.6×10^8	0.75	0.35	1.33
	[34]	Steady-state heat flow	[O] = 600, [Si] = 50, [C] = 500		0.80	0.30	1.54

0.09). The thermal conductivity shows a steep decrease from 152 W/m K ($x = 0$) to 21.5 W/m K ($x = 0.09$). Further decrease can be still seen for compositions up to $x = 0.2$. The samples of set 2 are with a high Al composition ($0.57 \leq x \leq 0.88$) and their thermal conductivity is in the range of 7–10 W/m K. In combination with data for HVPE-grown layers reported in our previous work [43] and for MOCVD grown layers reported by Daly *et al.* [38], we clearly see that the thermal conductivity does not show a remarkable change for the compositions of $0.2 \leq x \leq 0.9$. At the very high composition range of $0.9 \leq x \leq 1$, a steep increase of k with x is observed. In Fig. 3(a), the data measured by the 3ω method in HVPE-grown $\text{Al}_x\text{Ga}_{1-x}\text{N}$ layers [40] are also shown. These data, however, are significantly higher than all others reported. The reason for such discrepancy is not clear. However, it is worth noting that for layers examined in Ref. [40] an unexpected increase of the thermal conductivity with temperature is observed,

which is typical for amorphous or completely disordered materials [40].

In Fig. 3(a), the thermal conductivity calculated by the modified Callaway model (described in Sec. III) is also shown. The calculations are performed for layers with two different thicknesses ($0.5 \mu\text{m}$ and $2 \mu\text{m}$) and dislocation densities of $D_S = 4 \times 10^8 \text{ cm}^{-2}$ and $D_E = 4 \times 10^9 \text{ cm}^{-2}$, as well as for bulk dislocation-free $\text{Al}_x\text{Ga}_{1-x}\text{N}$. A good match between the theoretical and the experimental data for layers is observed. For the bulk $\text{Al}_x\text{Ga}_{1-x}\text{N}$, the lowest thermal conductivity ($k = 15.9 \text{ W/mK}$) is obtained at $x = 0.57$. This value is more than 15 times lower than the values for bulk GaN and AlN binary compounds.

To gain an insight on the composition dependence of the thermal conductivity of $\text{Al}_x\text{Ga}_{1-x}\text{N}$, we examine the individual contribution of different resistive phonon-scattering processes. The results for bulk $\text{Al}_x\text{Ga}_{1-x}\text{N}$ at 300 K are shown in Fig. 3(b). The contribution of the three-phonon umklapp scattering, which is known to dominate the thermal conductivity

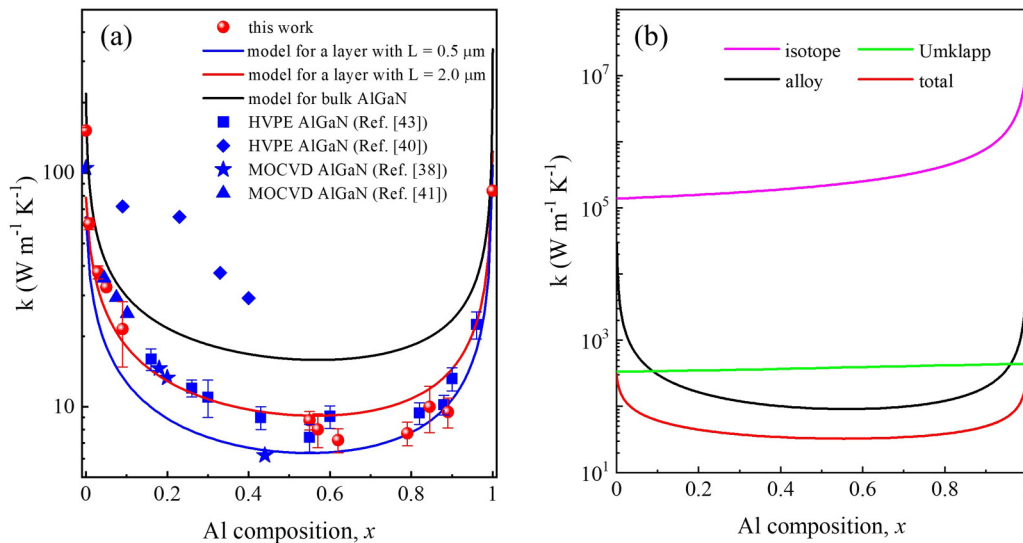


FIG. 3. (a) Measured (symbols) and calculated (lines) thermal conductivity of $\text{Al}_x\text{Ga}_{1-x}\text{N}$ at room temperature as a function of Al composition. Only data for nominally undoped layers are shown. (b) Composition dependence of the partial thermal conductivity calculated for each individual phonon-scattering process for bulk $\text{Al}_x\text{Ga}_{1-x}\text{N}$.

ity in binary semiconductor compounds at room temperature, is found to have a weak composition dependence. The specific composition dependence of the thermal conductivity of $\text{Al}_x\text{Ga}_{1-x}\text{N}$ is essentially due to the phonon-alloy scattering, where the fluctuations of atomic mass and atomic radius among the group-III atoms play a vital role. For Al compositions between $x = 0.1$ and $x = 0.95$, the phonon-alloy scattering gives the main contribution to the thermal conductivity. As for the phonon-isotope scattering, its contribution decreases at high Al composition because the Al atom has a single isotope. This can explain the slightly asymmetric composition dependence of the thermal conductivity. We note that the calculations for PD-, D-, and B-scattering processes, which could contribute to the thermal conductivity in epitaxial $\text{Al}_x\text{Ga}_{1-x}\text{N}$ layers, show a very weak composition dependence.

Using the modified Callaway model the thermal conductivity of $\text{Al}_x\text{Ga}_{1-x}\text{N}$ at temperatures well above the room temperature can be predicted. The composition dependence remains almost the same as that at room temperature but the values are significantly reduced. For example, we have found that for $2 \mu\text{m}$ thick $\text{Al}_x\text{Ga}_{1-x}\text{N}$ layers with compositions of $x = 0, 0.1$, and 0.6 the thermal conductivity at 1000 K is reduced by 50% , 31% , and 25% , respectively, compared to the values at 300 K . Note that the reduction becomes smaller with increasing composition up to $x = 0.6$ reflecting the decrease of the relative contribution of the three-phonon umklapp scattering in respect of that of the phonon-alloy scattering. At compositions $x > 0.6$ the temperature-induced reduction of the thermal conductivity between 300 K and 1000 K is increased due to the lower contribution of the phonon-alloy scattering and reaches 53% for $x = 1$ (AlN).

E. Effect of dislocations

In Fig. 4, the thermal conductivity of GaN and undoped $\text{Al}_x\text{Ga}_{1-x}\text{N}$ samples studied is plotted as a function the total dislocation density ($D = D_S + D_E$). A collection of published experimental data [18,43,86–89] is also shown in Fig. 4. Our data for GaN are fitted by the modified Callaway model where the dimensionless scaling factor on the right side of Eq. (12) is used as the only fitting parameter. The best fit is obtained for a scaling factor of 400 (red line in Fig. 4). The threshold dislocation density D_{th} (defined as the density at which the thermal conductivity of dislocation-free GaN decreases by 5%) is estimated to be $1.7 \times 10^8 \text{ cm}^{-2}$. A quite good agreement between our model and the published data (except for data in Ref. [18] and Ref. [86]) is observed. The thermal conductivity data for thick HVPE GaN measured by the 3ω method [18] show a much lower threshold dislocation density ($D_{th} = 1 \times 10^7 \text{ cm}^{-2}$). On the other hand, a surprising high thermal conductivity is measured by TDTR in MOCVD and molecular beam epitaxy grown GaN layers with dislocation density $> 2 \times 10^9 \text{ cm}^{-2}$ [89]. Li *et al.* [89] have speculated that the discrepancy between their data and those compiled in Ref. [18] is due to the size effect, i.e., due to the finite sample thickness and the contribution of the B scattering. However, it has been shown that the thermal conductivity of GaN measured in layers with different thicknesses tends to saturate at a thickness of $5\text{--}10 \mu\text{m}$ [43,90]. The thicknesses

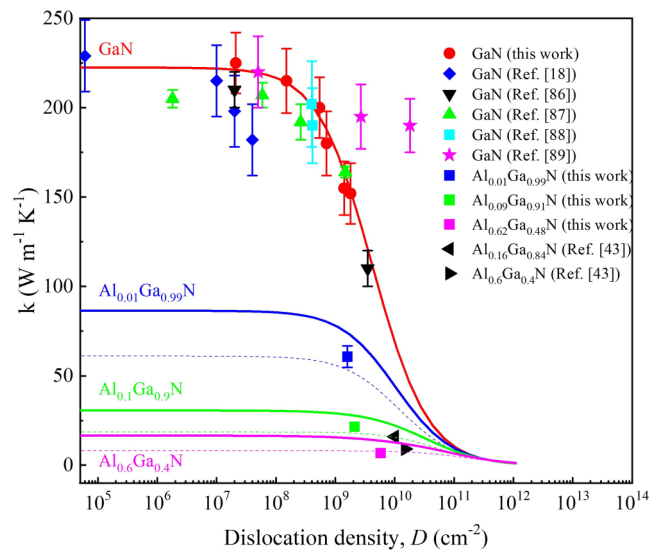


FIG. 4. Room-temperature thermal conductivity of studied GaN and $\text{Al}_x\text{Ga}_{1-x}\text{N}$ samples as a function of the total dislocation density ($D = D_S + D_E$). For a comparison, experimental data from Refs. [18,43,86–89] are also shown. The solid lines present the calculations using the modified Callaway model for bulk materials, while the dashed lines are the calculations for layers with thickness of $2 \mu\text{m}$.

of the samples examined by Mion *et al.* [18] as well as of the samples we have studied (except for sample AL0) are much larger, so any size effect can be excluded. We believe that the discrepancy between the data shown in Fig. 4 is mainly due to the way in which the dislocation density is determined. In Ref. [18], the dislocation density is estimated from panchromatic cathodoluminescence (CL) images meaning that only the dislocations which reach the surface are counted; then the total dislocation density is likely underestimated. Note that a large difference in the dislocation density determined by CL and XRD, especially in the range below $5 \times 10^7 \text{ cm}^{-2}$, is reported by Park and Bayram [87]. In Ref. [86], the dislocation density is determined from transmission electron microscopy (TEM) studies. TEM, however, is a local technique; i.e., the images are taken for a very small area. It is not clear where exactly the cross-section TEM images used for the dislocation density estimation in Ref. [86] are taken. Having in mind that the dislocation density varies strongly along the growth direction, the actual contribution of the D scattering to the thermal conductivity could be quite different.

Using a scaling factor of 400 on the right side of Eq. (12) the dislocation density dependence of thermal conductivity of $\text{Al}_x\text{Ga}_{1-x}\text{N}$ is calculated and shown in Fig. 4 for bulk materials (solid lines) and for $2 \mu\text{m}$ thick layers (dashed lines). It is found that the D_{th} in bulk $\text{Al}_x\text{Ga}_{1-x}\text{N}$ increases with the Al composition, reaching $1.1 \times 10^9 \text{ cm}^{-2}$ at $x = 0.6$. This can be explained by the increased contribution of the phonon-alloy scattering which prevails over the phonon-dislocation scattering at higher Al compositions. The D_{th} in $2 \mu\text{m}$ thick layers is higher than that in the bulk materials ($7 \times 10^9 \text{ cm}^{-2}$ at $x = 0.6$) due to the additional interplay with the phonon-boundary scattering. At Al composition above $x = 0.6$ (not shown here) the D_{th} decreases in both the bulk $\text{Al}_x\text{Ga}_{1-x}\text{N}$ and the layers

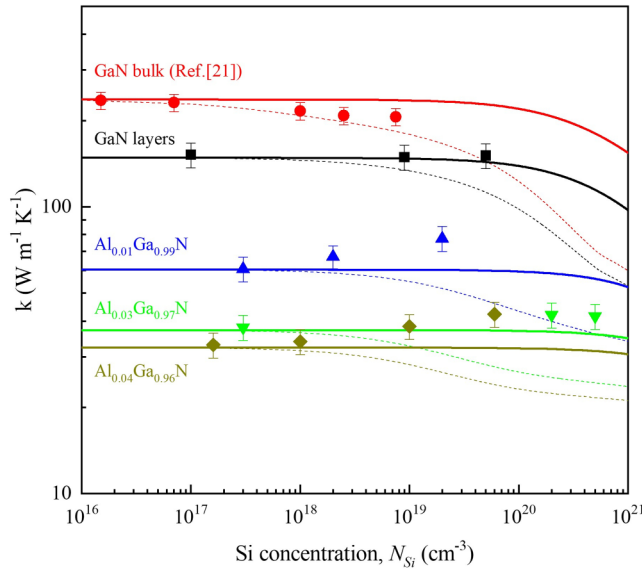


FIG. 5. Thermal conductivity of GaN and $\text{Al}_x\text{Ga}_{1-x}\text{N}$ as a function of Si doping concentration. The symbols show the experimental data while the solid (dashed) lines present calculations excluding (including) the FE scattering. Data for bulk GaN (Ref. [21]) are also shown.

as a result of the decreased contribution of the phonon-alloy scattering. As seen in Fig. 4, the experimental data for thermal conductivity of $\text{Al}_x\text{Ga}_{1-x}\text{N}$ layers is well aligned with the calculated dislocation density dependence. Unfortunately, there are no data for $D < 1 \times 10^9 \text{ cm}^{-2}$ because all samples studied so far are heteroepitaxial layers having a high density of dislocations.

F. Effect of Si doping

Figure 5 shows the thermal conductivity of Si-doped GaN and low Al composition $\text{Al}_x\text{Ga}_{1-x}\text{N}$ layers together with the doping concentration dependence predicted by the modified Callaway model. The solid lines present the calculations where the PD scattering is included in the model to render the effect of doping. In the PD-scattering process, the phonons are scattered by the mass and size difference between substitutional Si atoms and Ga host atoms. Dashed lines show the N_{Si} dependence when FE scattering due to the presence of free electrons from ionized Si donors is also taken into account. It is found that if only the PD scattering is accounted for in the model, the threshold Si concentration at which the doping starts to play a role on the thermal conductivity $N_{\text{Si,th}}$ (i.e., where the thermal conductivity of undoped GaN and $\text{Al}_x\text{Ga}_{1-x}\text{N}$ decreases by 5%) increases from $4.9 \times 10^{19} \text{ cm}^{-3}$ for bulk GaN to $8 \times 10^{19} \text{ cm}^{-3}$ for GaN layers, and to $9.6 \times 10^{20} \text{ cm}^{-3}$ for $\text{Al}_{0.04}\text{Ga}_{0.96}\text{N}$. With including the FE scattering the $N_{\text{Si,th}}$ is reduced by two orders of magnitude for GaN and $\text{Al}_{0.01}\text{Ga}_{0.99}\text{N}$ and even more for $\text{Al}_{0.03}\text{Ga}_{0.97}\text{N}$ and $\text{Al}_{0.04}\text{Ga}_{0.96}\text{N}$. These results can be explained by the interplay between different resistive phonon scattering processes. First, in GaN layers, the D- and B-scattering contributions prevail over that of the PD and FE scattering at $N_{\text{Si}} < 10^{19} \text{ cm}^{-3}$. Second, the

A scattering starts to dominate the thermal conductivity at Al composition $x > 0.01$. Third, the contribution of the FE-scattering slightly increases with the Al composition due to the increase of the electron effective mass and acoustic phonon deformation potential. Note that the calculations for GaN and $\text{Al}_x\text{Ga}_{1-x}\text{N}$ layers are done for a dislocation density of $1.5 \times 10^9 \text{ cm}^{-2}$ and layer thicknesses of $4 \mu\text{m}$ (GaN) and $2 \mu\text{m}$ ($\text{Al}_x\text{Ga}_{1-x}\text{N}$).

As seen in Fig. 5, experimental data for the thermal conductivity of bulk Si doped GaN (Ref. [21]) are well aligned with the calculations including both the PD and FE scattering. For GaN layers, however, our measurements reveal no reduction of k for Si concentration up to $5 \times 10^{19} \text{ cm}^{-3}$. It seems that the contribution of the FE scattering is overcome by another process leading to an increase of the thermal conductivity.

For $\text{Al}_x\text{Ga}_{1-x}\text{N}$ layers, the measured thermal conductivity follows the calculations for $N_{\text{Si}} < 10^{18}$. At higher Si doping, however, an increase of k is observed. At a doping concentration of 10^{20} cm^{-3} , an increase of 11% and 21% of k for compositions of $x = 0.03$ and $x = 0.04$, respectively, is observed. Obviously, the calculations of lattice thermal conductivity that include FD and FE scattering underestimate the experimental data in highly doped $\text{Al}_x\text{Ga}_{1-x}\text{N}$ layers. The increase of k is believed to be a result from the contribution of the electronic thermal conductivity, i.e., due to the thermal transport by the free electrons. Note that the free electrons are the primary carriers that transport the heat in metals. Therefore, they can have a substantial contribution to the thermal conductivity in heavily n -type doped semiconductors even at room temperature [91,92]. Comparing the calculations of the lattice thermal conductivity with the experimental data, we found that the relative contribution of the electronic thermal conductivity to the total thermal conductivity of $\text{Al}_x\text{Ga}_{1-x}\text{N}$ with compositions of $x = 0.03$ and $x = 0.04$ is about 37% and 48%, respectively. These large values of the relative contribution of the electronic thermal conductivity can be explained by (i) the reduction of the lattice thermal conductivity of $\text{Al}_{0.03}\text{Ga}_{0.97}\text{N}$ and $\text{Al}_{0.04}\text{Ga}_{0.96}\text{N}$ due to the phonon-alloy scattering (54% and 64%, respectively); (ii) the further drop of the lattice thermal conductivity due to the phonon-free-electron scattering at the free-electron concentration above 10^{20} cm^{-3} (about 33%); and (iii) the increased contribution of the free electrons to the heat transport [92].

G. Thermal boundary resistance at Au/ $\text{Al}_x\text{Ga}_{1-x}\text{N}$ interface

In our TTR measurements on thick $\text{Al}_x\text{Ga}_{1-x}\text{N}$ layers with Au transducer, we are able to extract not only the thermal conductivity of layers but also the TBR at Au/ $\text{Al}_x\text{Ga}_{1-x}\text{N}$ interface. To do that, in the processing of the acquired transients of the reflected signal, the thermal conductivity of $\text{Al}_x\text{Ga}_{1-x}\text{N}$ layer, and the Au/ $\text{Al}_x\text{Ga}_{1-x}\text{N}$ TBR were used as fitting parameters. The TBR results for all studied samples as a function of Al composition are shown in Fig. 6(a). The TBR for GaN and AlN layers is found to be quite small but for alloys a strong increase is observed. Note that the value of the Au/GaN TBR we obtain ($5.1 \text{ m}^2 \text{ K/GW}$) is in a good agreement with the previously reported data [93]. In Fig. 6(a) is also shown the root mean square (rms) surface roughness of

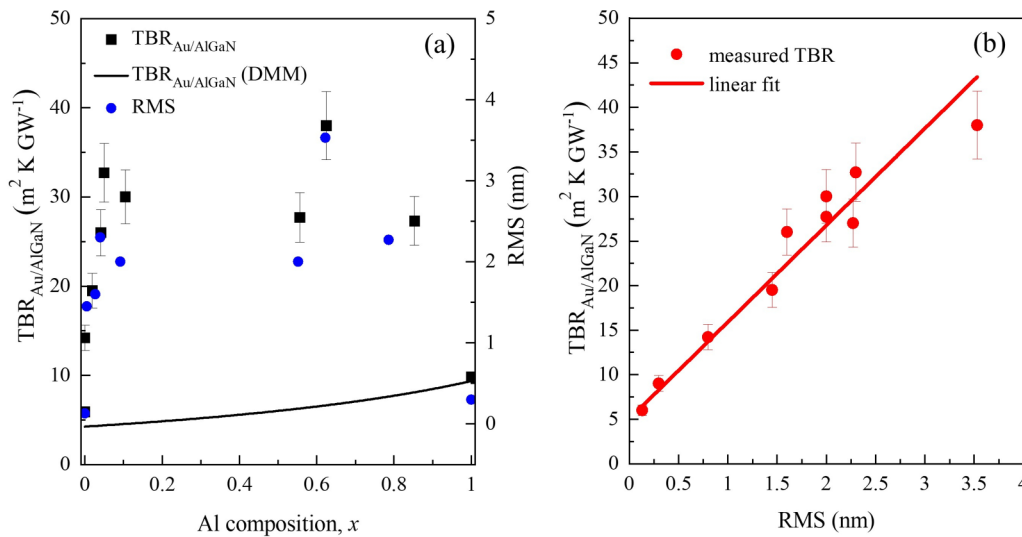


FIG. 6. (a) TBR at Au/Al_xGa_{1-x}N interface and rms of Al_xGa_{1-x}N layers as a function of Al composition. The solid line presents the TBR calculated by DMM model. (b) TBR as a function of rms.

Al_xGa_{1-x}N layers as measured by AFM. The clear correlation between the TBR and rms indicates that the increase of the TBR in alloys is rather due to the surface roughness and not to the internal material properties and the effect of Al alloying.

We have also performed calculations of the Au/Al_xGa_{1-x}N TBR based on the diffusive mismatch model (DMM) [94,95]. The DMM model that treats heat transport across the interface as diffusive, i.e., scattered phonons have no memory of the mode or directions, is found to be more appropriate for the metal/semiconductor TBR than the acoustic mismatch model especially at room temperature [95–97]. The results from calculations are shown by a solid line in Fig. 6(a). It is seen that the model predicts rather well the TBR for GaN and AlN but strongly underestimates the experimental data for the alloys. Note that the DMM model does not account for the phonon scattering due to the interface roughness. Generally, the model is valid when the dominant phonon wavelength $\lambda_d \leq \text{rms}$ [95]. We have estimated that for the Al_xGa_{1-x}N, λ_d at 300 K varies between 0.3 nm (GaN) and 0.45 nm (AlN). The rms of our GaN and AlN layers is in this range but for alloys the rms is much higher.

In Fig. 6(b), the Au/Al_xGa_{1-x}N TBR is plotted as a function of surface roughness. A linear increase of the TBR with increasing rms is observed. The linear fit of the experimental data yields $\text{TBR}(\text{m}^2 \text{K}/\text{GW}) = 5.1 + 10.8 \text{rms}(\text{nm})$. The high slope indicates that the TBR is very sensitive to the surface roughness. The intercept of the fitting line with the y axis (at about 5 m² K/GW) can be regarded as a low limit of Au/Al_xGa_{1-x}N TBR for an atomically flat interface.

V. CONCLUSION

Room-temperature thermal conductivity of Al_xGa_{1-x}N layers with Al composition $0 \leq x \leq 1$ has been measured using the TTR technique. The measured thermal conductivity was analyzed by numerical calculations within the frame of a modified Callaway's model. We have found a steep decrease

of the thermal conductivity of Al_xGa_{1-x}N with increasing Al composition in the range $0 \leq x \leq 0.2$ and with decreasing Al composition in the range of $0.9 \leq x \leq 1$ compared with the value for binary compounds. These observations are explained by the abrupt increase of the phonon-alloy scattering rate. For Al compositions between $x = 0.2$ and $x = 0.9$, the thermal conductivity is almost constant because the phonon-alloy scattering rate saturates in this region. We have also found that the dislocations have a detrimental effect on the thermal conductivity of layers. For GaN, the threshold dislocation density at which the thermal conductivity starts to decrease is estimated to be $1.7 \times 10^8 \text{ cm}^{-2}$. For Al_xGa_{1-x}N, the threshold dislocation density increases and reaches $1.1 \times 10^9 \text{ cm}^{-2}$ for the composition of $x = 0.6$ due to the prevailing contribution of the phonon-alloy scattering. For the Si-doped Al_xGa_{1-x}N layers we have revealed a sign of the electronic contribution to the thermal conductivity at carrier concentrations higher than 10^{18} cm^{-3} ; this leads to a higher thermal conductivity at higher doping concentration. The electronic contribution is estimated by 37% and 48% for the compositions of $x = 0.03$ and $x = 0.04$, respectively, at carrier concentration of 10^{20} cm^{-3} . Finally, we have studied the TBR at the Au/Al_xGa_{1-x}N interface and revealed that it is highly sensitive to the surface roughness of the Al_xGa_{1-x}N layers. The results from this study can be useful for the device optimization and the thermal management of the Al_xGa_{1-x}N-based electronic devices.

ACKNOWLEDGMENTS

The authors are indebted to Dr. P. Sukkaew for help in the growing of high Al content Al_xGa_{1-x}N layers, and Dr. J. H. Leach from Kyma Technologies, Inc., and Prof. T. Paskova from NCSU for providing the bulk HVPE GaN samples. This work was performed within the framework of the Center for III-Nitride Technology, C3NiT-Janzén, supported by the Swedish Governmental Agency for Innovation Systems (VINNOVA) under the Competence Center Program Grant

No. 2016-05190. We further acknowledge support from the Swedish Research Council under Grants No. 2016-00889 and No. 2017-03714, the Swedish Foundation for Strategic Research under Grants No. RIF14-055 and No. EM16-0024, and

the Swedish Government Strategic Research Area in Materials Science on Functional Materials at Linköping University, Faculty Grant SFO Mat LiU No. CBET-1336464 and Grant No. DMR-1506159.

-
- [1] J. Y. Tsao, S. Chowdhury, M. A. Hollis, D. Jena, N. M. Johnson, K. A. Jones, R. J. Kaplar, S. Rajan, C. G. V. de Walle, E. Bellotti, C. L. Chua, R. Collazo, M. E. Coltrin, J. A. Cooper, K. R. Evans, S. Graham, T. A. Grotjohn, E. R. Heller, M. Higashiwaki, M. S. Islam, P. W. Juodawlkis, M. A. Khan, A. D. Koehler, J. H. Leach, U. K. Mishra, R. J. Nemanich, R. C. N. Pilawa-Podgurski, J. B. Shealy, Z. Sitar, M. J. Tadjer, A. F. Witulski, M. Wraback, and J. A. Simmons, *Adv. Electron. Mater.* **4**, 1600501 (2018).
- [2] J. L. Hudgings, G. S. Simin, E. Santi, and M. A. Khan, *IEEE Trans. Power Electron.* **18**, 907 (2003).
- [3] B. J. Baliga, *Semicond. Sci. Technol.* **28**, 074011 (2013).
- [4] A. G. Baca, A. M. Armstrong, B. A. Klein, A. A. Allerman, E. A. Douglas, and R. J. Kaplar, *J. Vac. Sci. Technol. A* **38**, 020803 (2020).
- [5] T. Nanjo, M. Takeuchi, M. Suita, Y. Abe, T. Oishi, Y. Tokuda, and Y. Aoyagi, *Appl. Phys. Express* **1**, 011101 (2008).
- [6] Y. Wu, J. Zhang, S. Zhao, W. Zhang, Y. Zhang, X. Duan, J. Chen, and Y. Hao, *IEEE Electron Device Lett.* **40**, 1724 (2019).
- [7] A. G. Baca, B. A. Klein, J. R. Wendt, S. M. Lepkowski, C. D. Nordquist, A. M. Armstrong, A. A. Allerman, E. A. Douglas, and R. J. Kaplar, *IEEE Electron Device Lett.* **40**, 17 (2019).
- [8] H. Xue, C. H. Lee, K. Hussian, T. Razzak, M. Abdullah, Z. Xia, S. H. Sohel, A. Khan, S. Rajan, and W. Lu, *Appl. Phys. Express* **12**, 066502 (2019).
- [9] A. A. Allerman, A. M. Armstrong, A. Fischer, J. R. Dickerson, M. H. Crawford, M. P. King, M. W. Moseley, J. J. Wierer, and R. J. Kaplar, *Electron. Lett.* **52**, 1319 (2016).
- [10] R. Dalmau, H. S. Craft, R. Schlessler, S. Mita, J. Smart, G. P. C. Hitchcock, T. P. Chow, and B. Moody, *ECS Trans.* **80**, 217 (2017).
- [11] R. Gaska, A. Osinsky, J. W. Yang, and M. S. Shur, *IEEE Electron. Device Lett.* **19**, 89 (1998).
- [12] V. O. Turin and A. A. Baladin, *Electron. Lett.* **40**, 81 (2004).
- [13] J. Kuzmik, M. Tapajna, L. Valik, M. Molnar, D. Donoval, C. Fleury, D. Pogany, G. Strasser, O. Hilt, F. Brunner, and J. Wurfl, *IEEE Trans. Electron Devices* **61**, 3429 (2014).
- [14] X. Chen, S. Boumaiza, and L. Wei, *IEEE Trans. Electron Devices* **66**, 3748 (2019).
- [15] J. S. Lundh, B. Chatterjee, Y. Song, A. G. Baca, D. J. Kaplar, T. E. Beechem, A. A. Allerman, A. M. Armstrong, B. A. Klein, A. Bansal, D. Talreja, A. Pogrebnyakov, E. Heller, V. Gopalan, J. M. Redwing, B. M. Foley, and S. Choi, *Appl. Phys. Lett.* **115**, 153503 (2019).
- [16] B. Chatterjee, J. S. Lundh, Y. Song, D. Shoemaker, A. G. Baca, D. J. Kaplar, T. E. Beechem, C. Saltonstall, A. A. Allerman, A. M. Armstrong, B. A. Klein, A. Bansal, H. R. Seyf, D. Talreja, A. Pogrebnyakov, E. Heller, V. Gopalan, A. S. Henry, J. M. Redwing, B. M. Foley, and S. Choi, *IEEE Electron Device Lett.* **41**, 461 (2020).
- [17] G. A. Slack, L. J. Schowalter, D. Morelli, and J. A. Freitas Jr., *J. Cryst. Growth* **246**, 287 (2002).
- [18] C. Mion, J. F. Muth, E. A. Preble, and D. Hanser, *Appl. Phys. Lett.* **89**, 092123 (2006).
- [19] H. Shibata, Y. Waseda, H. Ohta, K. Kiyomi, K. Shimoyama, K. Fujito, H. Nagaoka, Y. Kagamitani, R. Simura, and T. Fukuda, *Mater. Trans.* **48**, 2782 (2007).
- [20] A. Jeżowski, O. Churiukova, J. Mucha, T. Suski, I. A. Obukhov, and B. A. Danilchenko, *Mater. Res. Express* **2**, 085902 (2015).
- [21] P. P. Paskov, M. Slomski, J. H. Leach, J. F. Muth, and T. Paskova, *AIP Adv.* **7**, 095302 (2017).
- [22] M. Slomski, L. Liu, J. F. Muth, and T. Paskova, in *Handbook of GaN Semiconductor Materials and Devices* (CRC Press, Boca Raton, 2017).
- [23] Q. Zheng, C. Li, A. Rai, J. H. Leach, D. A. Broido, and D. G. Cahill, *Phys. Rev. Mater.* **3**, 014601 (2019).
- [24] A. V. Inyushkin, A. N. Taldenkov, D. A. Chernodubov, V. V. Voronenkov, and Y. G. Shreter, *JETP Lett.* **112**, 106 (2020).
- [25] L. Lindsay, D. A. Broido, and T. L. Reinecke, *Phys. Rev. Lett.* **109**, 095901 (2012).
- [26] J. Ma, W. Li, and X. Luo, *J. Appl. Phys.* **119**, 125702 (2016).
- [27] K. Yuan, X. Zhang, D. Tang, and M. Hu, *Phys. Rev. B* **98**, 144303 (2018).
- [28] E. Minamitani, M. Ogura, and S. Watanabe, *Appl. Phys. Express* **12**, 095001 (2019).
- [29] R. B. Simon, J. Anaya, and M. Kuball, *Appl. Phys. Lett.* **105**, 202105 (2014).
- [30] P. Bagheri, P. Reddy, J. H. Kim, R. Rounds, T. Sochacki, R. Kirste, M. Bockowski, R. Collazo, and Z. Sitar, *Appl. Phys. Lett.* **117**, 082101 (2020).
- [31] R. Rounds, B. Sarkar, A. Klump, C. Hartmann, T. Nagashima, R. Kirste, A. Franke, M. Bickermann, Y. Kumagai, Z. Sitar, and R. Collazo, *Appl. Phys. Express* **11**, 071001 (2018).
- [32] R. L. Xu, M. M. Rojo, S. M. Islam, A. Sood, B. Vareskic, A. Katre, N. Mingo, K. E. Goodson, H. G. Xing, D. Jena, and E. Pop, *J. Appl. Phys.* **126**, 185105 (2019).
- [33] Z. Cheng, Y. R. Koh, A. Mamun, J. Shi, T. Bai, K. Huynh, L. Yates, Z. Liu, R. Li, E. Lee, M. E. Liao, Y. Wang, H. M. Yu, M. Kushimoto, T. Luo, M. S. Goorsky, P. E. Hopkins, H. Amano, A. Khan, and S. Graham, *Phys. Rev. Mater.* **4**, 044602 (2020).
- [34] A. V. Inyushkin, A. N. Taldenkov, D. A. Chernodubov, E. N. Mokhov, S. S. Nagalyuk, V. G. Ralchenko, and A. A. Khomich, *J. Appl. Phys.* **127**, 205109 (2020).
- [35] Y. R. Koh, Z. Cheng, A. Mamun, M. S. B. Hoque, Z. Liu, T. Bai, K. Hussain, M. E. Liao, R. Li, J. T. Gaskins, A. Giri, J. Tomko, J. L. Braun, M. Gaevski, E. Lee, L. Yates, M. S. Goorsky, T. Luo, A. Khan, S. Graham, and P. E. Hopkins, *ACS Appl. Mater. Interfaces* **12**, 29443 (2020).
- [36] M. Kazan, S. Pereira, M. R. Correia, and P. Masri, *Phys. Rev. B* **77**, 180302(R) (2008).
- [37] L. Lindsay, D. A. Broido, and T. L. Reinecke, *Phys. Rev. B* **87**, 165201 (2013).

- [38] B. C. Daly, H. J. Maris, A. V. Nurmikko, N. Kuball, and J. Han, *J. Appl. Phys.* **92**, 3820 (2002).
- [39] W. Liu and A. A. Balandin, *Appl. Phys. Lett.* **85**, 5230 (2004).
- [40] W. Liu and A. A. Balandin, *J. Appl. Phys.* **97**, 073710 (2005).
- [41] A. Filatova-Zalewska, Z. Litwicki, T. Suski, and A. Jezowski, *Solid State Sci.* **101**, 106105 (2020).
- [42] D. Q. Tran, N. Blumenschein, A. Mock, P. Sukkaew, H. Zhang, J. F. Muth, T. Paskova, P. P. Paskov, and V. Darakchieva, *Phys. B: Condens. Matter* **579**, 411810 (2020).
- [43] D. Q. Tran, R. Delgado-Carrascon, J. F. Muth, T. Paskova, M. Nawaz, V. Darakchieva, and P. P. Paskov, *Appl. Phys. Lett.* **117**, 252102 (2020).
- [44] S. Dagli, K. A. Mengle, and E. Kioupakis, [arXiv:1910.05440](https://arxiv.org/abs/1910.05440).
- [45] K. Takeda, M. Iwaya, T. Takeuchi, S. Kamiyama, and I. Akasaki, *Jpn. J. Appl. Phys.* **55**, 05FE02 (2016).
- [46] A. Kakanakova-Georgieva, R. R. Ciechonski, U. Forsberg, A. Lundskog, and E. Janzén, *Cryst. Growth Des.* **9**, 880 (2009).
- [47] D. Nilsson, E. Janzén, and A. Kakanakova-Georgieva, *Appl. Phys. Lett.* **105**, 082106 (2014).
- [48] S. Schöche, T. Hofmann, D. Nilsson, A. Kakanakova-Georgieva, E. Janzén, P. Kühne, K. Lorenz, M. Schubert, and V. Darakchieva, *J. Appl. Phys.* **121**, 205701 (2017).
- [49] T. Favaloro, J. Bahk, and A. Shakouri, *Rev. Sci. Instrum.* **86**, 024903 (2015).
- [50] R. Garrelts, A. Marconnet, and X. F. Xu, *Nanoscale Microscale Thermophys. Eng.* **19**, 245 (2015).
- [51] S. Lee, S. Y. Know, and H. J. Ham, *Jpn. J. Appl. Phys.* **50**, 11RG02 (2011).
- [52] Y. S. Touloukian and E. H. Buyco, *Thermophysical Properties of Matter, The TPRC Data Series, Vol. 5, Specific Heat of Nonmetallic Solids* (Plenum, New York, 1970).
- [53] D. A. Broido, M. Malorny, G. Birner, N. Mingo, and D. A. Stewart, *Appl. Phys. Lett.* **91**, 231922 (2007).
- [54] J. Callaway, *Phys. Rev.* **113**, 1046 (1959).
- [55] M. G. Holland, *Phys. Rev.* **132**, 2461 (1963).
- [56] M. Asen-Palmer, K. Bartkowski, E. Gmelin, M. Cardona, A. P. Zhernov, A. V. Inyushkin, A. Taldenkov, V. I. Ozhogin, K. M. Itoh, and E. E. Haller, *Phys. Rev. B* **56**, 9431 (1997).
- [57] D. T. Morelli, J. P. Heremans, and G. A. Slack, *Phys. Rev. B* **66**, 195304 (2002).
- [58] C. Herring, *Phys. Rev.* **95**, 954 (1954).
- [59] P. G. Klemens, *Proc. Phys. Soc. A* **68**, 1113 (1955).
- [60] J. Zou, D. Kotchetkov, A. A. Balandin, D. I. Florescu, and P. H. Pollak, *J. Appl. Phys.* **92**, 2534 (2002).
- [61] T. E. Beechem, A. E. McDonald, E. J. Fuller, A. A. Talin, C. M. Rost, J. P. Maria, J. T. Gaskins, P. E. Hopkins, and A. A. Allerman, *J. Appl. Phys.* **120**, 095104 (2016).
- [62] B. Abeles, *Phys. Rev.* **131**, 1906 (1963).
- [63] S. Adachi, *J. Appl. Phys.* **54**, 1844 (1983).
- [64] H. Angerer, D. Brunner, F. Freudenberg, O. Ambacher, M. Stutzmann, R. Höppler, T. Metzger, E. Born, G. Dollinger, A. Bergmaier, S. Karsch, and H. J. Körner, *Appl. Phys. Lett.* **71**, 1504 (1997).
- [65] E. A. Albanesi, W. R. L. Lambrecht, and B. Segall, *Phys. Rev. B* **48**, 17841 (1993).
- [66] J. M. Ziman, *Philos. Mag.* **1**, 191 (1956).
- [67] J. M. Ziman, *Philos. Mag.* **2**, 292 (1957).
- [68] R. Berman, F. E. Simon, and J. M. Ziman, *Proc. R. Soc. London A* **220**, 171 (1953).
- [69] R. Berman, F. L. Foster, and J. M. Ziman, *Proc. R. Soc. London A* **231**, 130 (1955).
- [70] E. Ziade, J. Yang, G. Brummer, D. Nothorn, T. Moustakas, and A. J. Schmidt, *Appl. Phys. Lett.* **110**, 031903 (2017).
- [71] H. Morkoc, *Handbook of Nitride Semiconductors and Devices, Vol. 1, Materials Properties, Physics and Growth* (Wiley-VCH, Weinheim, 2008).
- [72] V. Darakchieva, B. Monemar, and A. Usui, *Appl. Phys. Lett.* **91**, 031911 (2007).
- [73] W. Paszkowicz, S. Podsiadlo, and R. Minikayev, *J. Alloys Compd.* **382**, 100 (2004).
- [74] N. Nakamura, H. Ogi, and M. Hirao, *J. Appl. Phys.* **111**, 013509 (2012).
- [75] Y. Ohashi, M. Arakawa, J. Kushibiki, B. M. Epelbaum, and A. Winnacker, *Appl. Phys. Express* **1**, 077004 (2008).
- [76] T. Ruf, J. Serrano, M. Cardona, P. Pavone, M. Pabst, M. Krisch, M. D'Astuto, T. Suski, I. Grzegory, and M. Leszczynski, *Phys. Rev. Lett.* **86**, 906 (2001).
- [77] M. Schwoerer-Böhning, A. T. Macrander, M. Pabst, and P. Pavone, *Phys. Status Solidi B* **215**, 177 (1999).
- [78] I. Vurgaftman and J. R. Meyer, *J. Appl. Phys.* **94**, 3675 (2003).
- [79] H. Morkoc, *Nitride Semiconductor Devices: Fundamentals and Applications* (Wiley-VCH, Weinheim, 2013).
- [80] F. Oehler, M. E. Vickers, M. J. Kappers, C. J. Humphreys, and R. A. Oliver, *Jpn. J. Appl. Phys.* **52**, 08JB29 (2013).
- [81] T. Metzger, R. Höppler, E. Born, O. Ambacher, M. Stutzmann, R. Stömmmer, M. Schuster, H. Göbel, S. Christiansen, M. Albrecht, and H. P. Strunk, *Philos. Mag. A* **77**, 1013 (1998).
- [82] S. R. Lee, A. M. West, A. A. Allerman, K. E. Waldrip, D. M. Follstaedt, P. P. Provencio, D. D. Koleske, and C. R. Abernathy, *Appl. Phys. Lett.* **86**, 241904 (2005).
- [83] H. Iwanaga, A. Kunishige, and S. Takeuchi, *J. Mater. Sci.* **35**, 2451 (2000).
- [84] R. J. Bruls, H. T. Hintzen, G. de With, R. Metselaar, and J. C. van Miltenburg, *J. Phys. Chem. Solids* **62**, 783 (2001).
- [85] C. Bungaro, K. Rapcewicz, and J. Bernholc, *Phys. Rev. B* **61**, 6720 (2000).
- [86] D. I. Florescu, V. M. Asnin, F. H. Pollak, A. M. Jones, J. C. Ramer, M. J. Schurman, and I. Ferguson, *Appl. Phys. Lett.* **77**, 1464 (2000).
- [87] K. Park and C. Bayram, *J. Appl. Phys.* **126**, 185103 (2019).
- [88] R. D. Carrascon, D. Q. Tran, P. Sukkaew, A. Mock, R. Ciechonski, J. Ohlsson, Y. Zhu, O. Hultin, B. Monemar, P. P. Paskov, L. Samuelson, and V. Darakchieva, *Phys. Status Solidi B* **257**, 1900581 (2020).
- [89] H. Li, R. Hanus, C. A. Polanco, A. Zeidler, G. Koblmüller, Y. K. Koh, and L. Lindsay, *Phys. Rev. B* **102**, 014313 (2020).
- [90] T. Wang, J. Carrete, N. Mingo, and G. K. H. Madsen, *ACS Appl. Mater. Interfaces* **11**, 8175 (2019).
- [91] C. M. Bhandari and D. M. Rowe, *Appl. Phys. A* **37**, 175 (1985).
- [92] W. Liu and A. A. Balandin, *J. Appl. Phys.* **97**, 123705 (2005).
- [93] B. F. Donovan, C. J. Szejewski, J. C. Duda, R. Cheaito, J. T. Gaskins, C. Y. P. Yang, C. Constantin, R. E. Jones, and P. E. Hopkins, *Appl. Phys. Lett.* **105**, 203502 (2014).
- [94] E. T. Swartz and R. O. Pohl, *Rev. Mod. Phys.* **61**, 605 (1989).
- [95] P. E. Phelan, *J. Heat Transfer* **120**, 37 (1998).
- [96] P. E. Hopkins, P. M. Norris, and R. J. Stevens, *J. Heat Transfer* **130**, 022401 (2008).
- [97] C. Monachon, L. Weber, and C. Dames, *Annu. Rev. Mater. Res.* **46**, 433 (2016).